



Cite this: RSC Adv., 2017, 7, 53306

## Controllable growth of $\text{Na}_2\text{CO}_3$ fibers for mesoporous activated alumina ball modification towards the high-efficiency adsorption of HCl gas at low temperature

Shuoyang Liang,<sup>a</sup> Zhengyun Fan,<sup>b</sup> Weidong Zhang,<sup>b</sup> Min Guo,<sup>a</sup> Fangqin Cheng<sup>c</sup> and Mei Zhang  <sup>\*ac</sup>

To fundamentally solve the problem of chlorine corrosion in blast furnace gas (BFG) systems, a supported adsorbent is used for HCl removal at low temperature. In this paper, three alkaline substances,  $\text{Ca}(\text{OH})_2$ ,  $\text{NaOH}$ , and  $\text{Na}_2\text{CO}_3$ , were separately coated on the surface of activated alumina balls (AABs) by wetness impregnation method, using the as-active components. These materials were measured by XRF, XRD, SEM, TEM, and  $\text{N}_2$  adsorption to characterize textural properties. The modification experiments indicated that  $\text{Na}_2\text{CO}_3$  fibers can be obtained on the surface of AABs by adjusting the loading amounts, impregnation time, and drying conditions. The fibers' structure contributes to the gas phase diffusion in the product layer, greatly improving the conversion of  $\text{Na}_2\text{CO}_3$  ( $>0.98$ ). The highest value of HCl adsorption capacity reaches  $3.56 \text{ mmol g}^{-1}$  when the  $\text{Na}_2\text{CO}_3$  loading amount is 20 wt%, five times the adsorption capacity of pure AABs. The kinetics of HCl removal by the  $\text{Na}_2\text{CO}_3$  fiber-modified AABs is controlled by the interfacial chemical reaction.

Received 29th September 2017  
Accepted 6th November 2017

DOI: 10.1039/c7ra10790k

rsc.li/rsc-advances

### 1. Introduction

It has been widely accepted that blast furnace gas (BFG) is a reusable derivative energy source due to the large heat and high pressure in the process of blast furnace production.<sup>1</sup> In the process of recycling the blast furnace gas, the dry-dedusting process is adopted to make the gas purification efficient. However, serious corrosion has appeared in the BFG pipeline in the short term—a large amount of salt blocks the Blast Furnace Top Gas Recovery Turbine Unit (TRT), and even the refractory bricks in the hot blast stove have been partially broken.<sup>2</sup> According to the reports, hydrogen chloride (HCl) in the gas stream is the only explanation for equipment corrosion.<sup>2,3</sup> Normally, the temperature of BFG is in the range of 380–423 K. BFG steam consists of 23%  $\text{CO}$ , 20%  $\text{CO}_2$ , 55%  $\text{N}_2$ , and a small amount of methane; simultaneously, there is about 300 ppm hydrogen chloride (HCl). Although the content of HCl in the BFG is very small, the blast furnace still generates a heavy chlorine burden attributed to the large amount of blast furnace gas production. For example, a 2650  $\text{m}^3$  BF produces 8 million  $\text{m}^3$  of BFG per day, containing about 3 tons of HCl, which is

a huge threat to the gas pipeline and hot blast stove. Therefore, finding an effective adsorption material to remove HCl from the BFG is urgently necessary.

At present, more studies have paid attention to the removal of acid gases from the hot flue gas (673–1073 K) of the coal industry.<sup>4–11</sup> The reaction mechanism mainly depends on the neutralization of acid and alkali to capture acid gas in the process of gas stream cleaning. Duo *et al.*<sup>5,12</sup> reported that the higher HCl capacity of sorbents correspond to the higher temperature from 573 to 873 K. Na sorbents showed optimal HCl sorption performance in the temperature range of 673–773 K. Dou *et al.*<sup>13,14</sup> found that  $\text{Na}_2\text{CO}_3$ ,  $\text{Ca}(\text{OH})_2$ , or  $\text{CaO}$  were suitable to achieving the tolerance limit of 1 ppmv HCl from hot gas. The experimental results showed that the HCl capacity of alkali materials at 473 K is less than 20% ( $3.5 \text{ mmol HCl g}^{-1}$ ) of that at 773 K, suggesting that the chemical reaction of adsorbents is limited at low temperature.<sup>15</sup> Besides, with poor structure, the conversion of the active materials is less than 50%,<sup>16</sup> which undoubtedly increases the cost of dechlorination.

Mesoporous materials such as activated carbon (AC), activated alumina balls (AABs), molecular sieves, *etc.* have been developed as potential adsorbents or catalyst supports for the removal of acidic gases due to their large surface area and abundant porous structure.<sup>17–21</sup> Taguchi *et al.*<sup>22–24</sup> pointed out that the reaction mechanism of gas on the surface of these porous materials relies on physical adsorption, which contributes to regeneration and recycling.  $\text{ZnO}$  supported by 3-D structural mesoporous molecular

<sup>a</sup>School of Metallurgical and Ecological Engineering, University of Science and Technology Beijing, Beijing 100083, China. E-mail: zhangmei@ustb.edu.cn; Fax: +86 10 62334926

<sup>b</sup>Institute of Technology of Shougang Group, Beijing 100043, China

<sup>c</sup>Shanxi Collaborative Innovation Center of High Value-added Utilization of Coal-related Wastes in Shanxi University, China



sieves had been synthesized for  $\text{H}_2\text{S}$  removal from gas stream, reported by Li,<sup>25</sup> suggesting that the mesoporous structure benefited the dispersion of active phase. Among them, activated alumina balls (AABs) are well known as a potential carrier material for the adsorption of acid gases at low temperature due to their receptivity to modification with alkaline substances.<sup>26–29</sup>

For gases at room temperature, alkaline substances are usually used as active materials, supported by impregnation method, to remove acid gas for feeding molten carbonate fuel cells (MCFCs).<sup>30–33</sup> Lee<sup>34</sup> showed that the HCl capacity of NaOH/AC is about 6 times that of commercial alumina. However, Micoli *et al.*<sup>35,36</sup> investigated the HCl adsorption performance of activated carbon impregnated with KOH, NaOH or  $\text{Na}_2\text{CO}_3$ , respectively. They suggested that the best adsorption performance for HCl adsorption was obtained by impregnating  $\text{Na}_2\text{CO}_3$ . Due to temperature limits, the chlorine capacity of the sorbent was lower than  $0.4 \text{ mmol HCl g}^{-1}$ . Zhao *et al.*<sup>37–39</sup> suggested that  $\text{K}_2\text{CO}_3/\text{Al}_2\text{O}_3$  and  $\text{Na}_2\text{CO}_3/\text{Al}_2\text{O}_3$  had the potential to be employed as excellent sorbents for  $\text{CO}_2$  uptake due to their rapid reaction rate and high  $\text{CO}_2$  capture capacities. Zhao<sup>40</sup> investigated the effect of  $\text{Na}_2\text{CO}_3$  loading on the adsorption capacity of the acid gases, which reached a maximum at the dispersion threshold. The paper of Dong<sup>41</sup> showed that there was a change of surface structure after the modification of  $\gamma\text{-Al}_2\text{O}_3$  with  $\text{Na}_2\text{CO}_3$ , unfortunately without any further analysis. It is worth mentioning that the change of HCl concentration in mixed gas has little effect on the adsorption capacity in the adsorption test.<sup>5,34</sup> Therefore, many experiments to simulate the removal of HCl from gas tend to adopt an accelerated aging test with high HCl concentration.

In general, there is a lack of literature on HCl removal from BFG in the steel industry for its extreme conditions, namely, selective removal of HCl at the lower temperature of 380–423 K. For the purpose of environmental protection and energy recovery, the importance of HCl removal from blast furnace gas is self-evident. In this work, three modifiers,  $\text{Na}_2\text{CO}_3$ ,  $\text{Ca}(\text{OH})_2$  and NaOH, were coated on AABs by impregnation method. The structure properties of the initial, impregnated and exhausted materials have been characterized. The adsorption activity of the prepared materials had been measured using the accelerated aging test with a HCl concentration of 50% at the low temperature of 423 K; accordingly, the reaction mechanism of HCl and sorbents are also proposed.

## 2. Experimental

### 2.1 Materials

Commercial activated alumina balls (AABs) were purchased from Shandong province in China without further purification. Calcium hydroxide ( $\text{Ca}(\text{OH})_2$ ), sodium carbonate anhydrous ( $\text{Na}_2\text{CO}_3$ ), and sodium hydroxide (NaOH) were analytical grade and used as received without further purification. The basic physical properties of AABs are shown in Table 1.

### 2.2 Preparation of modified sorbents

The modified sorbents in this study were prepared by the impregnation method. The preparation process consisted of

Table 1 The physical properties of AABs

Properties	Particle size (mm)	$S_{\text{BET}}$ ( $\text{m}^2 \text{ g}^{-1}$ )	Pore volume ( $\text{cm}^3 \text{ g}^{-1}$ )	Pore size (nm)
Parameter	4–8	160	0.45	9.74

two stages, namely, the selection of modifiers and optimization of impregnating conditions.

**2.2.1 Alkaline modifier selection.** The impregnation solutions were obtained by dissolving 0.34 g  $\text{Ca}(\text{OH})_2$  powder, 20 g NaOH powder and 20 g  $\text{Na}_2\text{CO}_3$  powder in 200 mL of deionized water, respectively, to form three kinds of impregnation solutions. Then, 40 g AABs were severally added into the impregnation solutions, which were then subjected to ultrasonic shocking at room temperature for 1 h, immersion for 17 h and finally drying at 473 K for 24 h. The obtained samples were named  $\text{Ca}(\text{OH})_2\text{-AAB}$ , 10NaOH-AAB, and 10 $\text{Na}_2\text{CO}_3$ -AAB, respectively; 10 represents the designed loading amounts of NaOH and  $\text{Na}_2\text{CO}_3$ , whereas the loading amount of  $\text{Ca}(\text{OH})_2$  is the maximum value for its lower solubility. The pure AABs without alkaline modification were used for comparison. The actual loading amounts of NaOH and  $\text{Na}_2\text{CO}_3$  on the sorbents were determined by X-ray fluorescence (XRF).

**2.2.2 Impregnation parameters selection.** In order to optimize the microstructure of sorbents, factors such as loading amounts of  $\text{Na}_2\text{CO}_3$ , impregnation time and drying time have been investigated; the details of influencing factors are shown in Table 2. To prepare the impregnation solution, 10 g, 30 g, 40 g, 50 g and 60 g pure  $\text{Na}_2\text{CO}_3$  powder were separately placed in 200 mL of deionized water resulting in, respectively,  $0.47 \text{ mol L}^{-1}$ ,  $1.42 \text{ mol L}^{-1}$ ,  $1.88 \text{ mol L}^{-1}$ ,  $2.36 \text{ mol L}^{-1}$  and  $2.83 \text{ mol L}^{-1}$   $\text{Na}_2\text{CO}_3$  solutions, and five sorbents of different  $\text{Na}_2\text{CO}_3$  loading amounts were obtained after 40 g AABs had been impregnated in the corresponding  $\text{Na}_2\text{CO}_3$  solution. The designations of 5, 15, 20, 25 and 30 correspond to the percentage of  $\text{Na}_2\text{CO}_3$  loading amounts. The effects of the impregnation time (2 h, 10 h, 17 h and 24 h) and drying time (16 h, 20 h, 24 h and 28 h) on the microstructure of sorbents were subsequently investigated. The actual loading amounts of  $\text{Na}_2\text{CO}_3$  on the sorbents were determined by XRF.

### 2.3 Activity test of HCl removal

After the preparation of modified sorbent loaded with  $\text{Na}_2\text{CO}_3$ , its HCl removal activity was subsequently tested in a fixed bed reactor with the reaction temperature of 423 K under normal atmosphere. The experimental apparatus is shown in Fig. 1. The sorbents were firstly treated at 423 K for 0.5 h in  $\text{N}_2$  flow

Table 2 Summary of impregnation conditions

Modifier	Factors	Parameters
$\text{Na}_2\text{CO}_3$	Loading amounts	5%, 15%, 20%, 25%
	Impregnation time	2 h, 10 h, 17 h, 24 h
	Drying time	16 h, 20 h, 24 h, 28 h



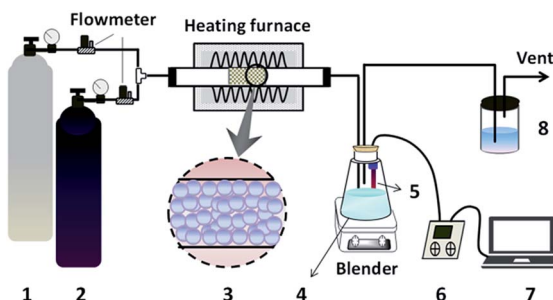


Fig. 1 Schematic diagram of the experimental apparatus: 1-N<sub>2</sub> cylinder, 2-HCl cylinder, 3-sorbents, 4-adsorption bottle, 5-pH electrode, 6-pH meter, 7-computer, 8-treatment bottle.

(20 mL min<sup>-1</sup>) before the test. High-purity HCl and N<sub>2</sub>, whose flow rates were similarly controlled by mass flow meters at 20 mL min<sup>-1</sup>, were mixed to pass through the sorbents (about 23 g) in the heating furnace. Because the work temperature of BFG is in the range of 380–423 K, the experimental temperature for HCl adsorption was controlled at 423 K to simulate the real temperature of BFG. Afterwards, the escaped HCl was absorbed by 1 L deionized water in the adsorption bottle, and the concentration  $C_t$  of HCl in the outlet gas at that moment was ascertained synchronously by detecting the change of the pH value in the adsorption solution.<sup>35,36,42</sup> Finally, the gas stream flowed through the treatment bottle, ensuring no pollution to the environment before the vent.

The test was stopped immediately when the pH value decreased sharply in the adsorption bottle; this moment was named the breakthrough time  $t_b$ . The exhausted sorbents were taken out of the reactor and desorbed in the deionized water, and the concentration  $C_e$  of chloride ion in the desorption solution was determined by a chloride ion concentration meter.

The HCl adsorption capacity  $q_e$  (mmol g<sup>-1</sup>) of the exhausted sorbents can be calculated from the following eqn (1):

$$q_e = \frac{VC_e}{m_0} \times 1000 \quad (1)$$

where  $m_0$  (g) is the initial mass of sorbents,  $V$  (L) is the volume of the desorption solution, and  $C_e$  (mol L<sup>-1</sup>) is the concentration of Cl<sup>-</sup> in the desorption solution at equilibrium.

The adsorption efficiency  $\eta$  of the sorbents at every moment can be calculated using the following eqn (2):

$$\eta = \frac{1 - C_t}{C_0} \times 100\% \quad (2)$$

where  $C_0$  (constant, 20 mL min<sup>-1</sup>) represents the concentration of HCl in the inlet gas, and  $C_t$  (mL min<sup>-1</sup>) represents the concentration of HCl in the outlet gas at time  $t$ .

#### 2.4 Characterizations

The actual loading amounts of Na<sub>2</sub>CO<sub>3</sub> supported on the sorbents were determined by X-ray fluorescence spectrometer (XRF-1800, Japan). The field emission scanning electron microscope (FESEM) (Zeiss supra 55), operated at 10 kV, coupled with energy dispersive X-ray analysis (EDS) was used to

investigate the morphologies and element distribution of sorbent nanostructures. The X-ray diffraction (XRD) analysis, carried out on a powder X-ray diffractometer (Rigaku Dmax-2500 diffractometer using Cu K $\alpha$  radiation), was used to determine the phase composition of the sorbents. Further structural characterization of the Na<sub>2</sub>CO<sub>3</sub> fibers coated on the AABs substrate was performed by applying high-resolution transmission electron microscopy (HRTEM, Tecnai F20) operated at 200 kV. Surface area measurements were carried out by N<sub>2</sub> adsorption at 77 K using a Micromeritics ASAP2020 instrument. The pH value of the adsorption solution was monitored by pH electrode 201T-M connected to the pH meter (MP520, Shanghai, San-Xin). The chloride ion concentration in the HCl desorption solution was measured by chloride ion-selective electrode CL502 connected concentration meter (MP523, Shanghai, San-Xin).

## 3 Results and discussion

### 3.1 Preparation of the alkaline modified sorbents

**3.1.1 Selection of modifier.** Three alkali-modified sorbents, namely, Ca(OH)<sub>2</sub>-AAB, 10NaOH-AAB and 10Na<sub>2</sub>CO<sub>3</sub>-AAB, were characterized by SEM, XRD and BET. The loading amounts and BET results are summarized in Table 3. It can be observed that the loading amount of Na<sub>2</sub>CO<sub>3</sub> is the same as NaOH. However, the amount of Ca(OH)<sub>2</sub> impregnated was less than 1 wt%. The BET results showed that the specific surface area and pore volume of 10NaOH-AAB were greatly reduced. In contrast, the sample 10Na<sub>2</sub>CO<sub>3</sub>-AAB retained the specific surface area after loading with Na<sub>2</sub>CO<sub>3</sub> solution.

The XRD patterns of the modified samples are shown in Fig. 2. It depicts that sample Ca(OH)<sub>2</sub>-AAB shows corresponding characteristic peaks of the substrate, whereas sample 10NaOH-AAB shows trace peaks of NaAlO<sub>2</sub> compared with the obvious peaks of Na<sub>2</sub>CO<sub>3</sub> phase in sample 10Na<sub>2</sub>CO<sub>3</sub>-AAB besides the substrate, suggesting that a complex reaction between NaOH and the AAB substrate has occurred.

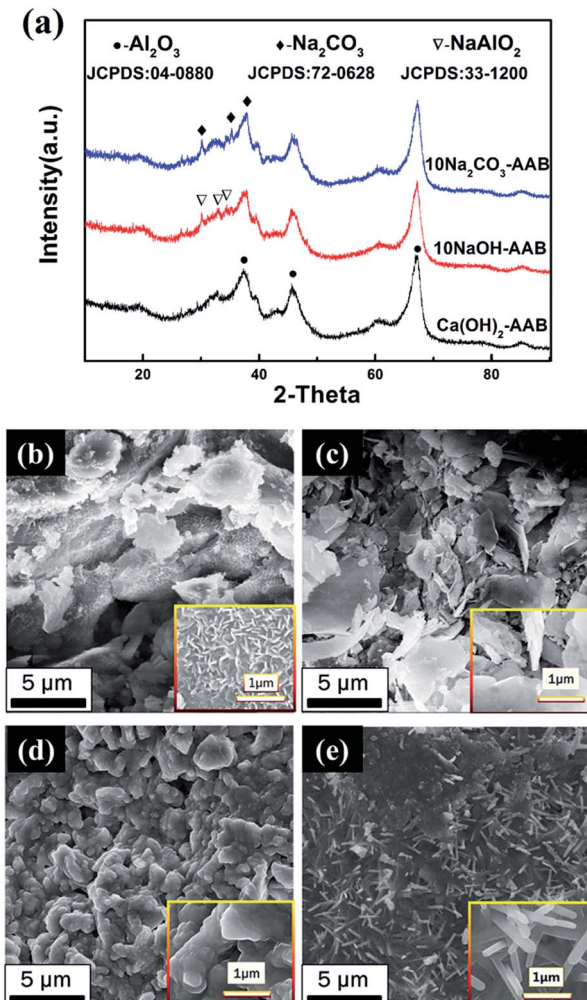
The SEM images of the untreated and modified AABs with alkaline substances are shown in Fig. 2(b–e). From Fig. 2(b), it can be seen that there were a large number of fluffy structures on the surface of the original AABs, which makes its specific surface area large and benefits the alkaline adsorption. The modification of Ca(OH)<sub>2</sub> as presented in Fig. 2(c) generates some lamellar structures in the AABs. However, the modification of NaOH deteriorates the surface morphology of alumina balls; namely, the pores in the AABs are almost blocked (Fig. 2(d)). The microscopic morphology of sorbent 10Na<sub>2</sub>CO<sub>3</sub>-AAB is shown in Fig. 2(e); a layer of fibrous network coats the surface of AABs, indicating that the Na<sub>2</sub>CO<sub>3</sub> fibers on the support help to preserve its high surface area. Considering the surface morphology and physical properties of the sorbent after modification, Na<sub>2</sub>CO<sub>3</sub> has been selected as the optimal modifier.

**3.1.2 Effect of Na<sub>2</sub>CO<sub>3</sub> loading amount.** The relationship curve of the actual loading amounts of Na<sub>2</sub>CO<sub>3</sub> on the sorbents with the designed loading amounts is shown in Fig. 3(a). The actual loading amount of Na<sub>2</sub>CO<sub>3</sub> increased synchronously with



Table 3 The loading amounts and BET results of the AABs with or without modification

Samples	AAB	Ca(OH) <sub>2</sub> -AAB	10NaOH-AAB	10Na <sub>2</sub> CO <sub>3</sub> -AAB
Designed loading amount (wt%)	—	0.34	10	10
Loading amount (wt%)	—	5	98	98
$S_{BET}$ (m <sup>2</sup> g <sup>-1</sup> )	160	125	105	144
Pore volume (cm <sup>3</sup> g <sup>-1</sup> )	0.45	0.51	0.40	0.51
Pore diameter (nm)	9.74	6.59	9.32	7.9

Fig. 2 (a) XRD patterns of the modified sorbents with different alkaline substances. The SEM images of the untreated and modified sorbents: (b) AABs, (c) Ca(OH)<sub>2</sub>-AAB, (d) 10NaOH-AAB and (e) 10Na<sub>2</sub>CO<sub>3</sub>-AAB.

the increasing concentration of Na<sub>2</sub>CO<sub>3</sub> solution up to 20 wt%, and then it continued to increase, but slowly.

Moreover, the actual loading capacities are almost accorded to the concentration of Na<sub>2</sub>CO<sub>3</sub> solution when it is lower than 25 wt%, indicating that the loading amount of Na<sub>2</sub>CO<sub>3</sub> in the sorbents reached saturation herein. Therefore, the loading amounts ranging from 5 wt% to 25 wt% is suitable for further investigation.

The XRD patterns of different loading amounts are shown in Fig. 3(b). When the loading amount reaches 10 wt%, the slight characteristic peaks of Na<sub>2</sub>CO<sub>3</sub> can be detected in the XRD

patterns. When the loading amount increases to 15 wt% and even higher, the characteristic peaks of Na<sub>2</sub>CO<sub>3</sub> are obvious. There is no new phase formation in the entire process, indicating that no chemical reaction happened between Na<sub>2</sub>CO<sub>3</sub> and AABs. The BET results of the samples with different loading amounts are listed in Table 4. It shows that the specific surface area of the sorbent decreases first and then increases with the increasing loading amounts, and reaches the highest value of 150 m<sup>2</sup> g<sup>-1</sup> when loading amount is 15 wt%. The specific surface area of the sorbent obviously reduces when the loading amount is further increased to 25 wt%, suggesting that there must be a great change in AAB microstructure.

The FESEM images of modified AABs with different loading amounts of Na<sub>2</sub>CO<sub>3</sub> are shown in Fig. 4(a-d). Clearly, the surface morphology of the samples changes greatly with different loading amounts. When the loading amount is 5 wt%, the

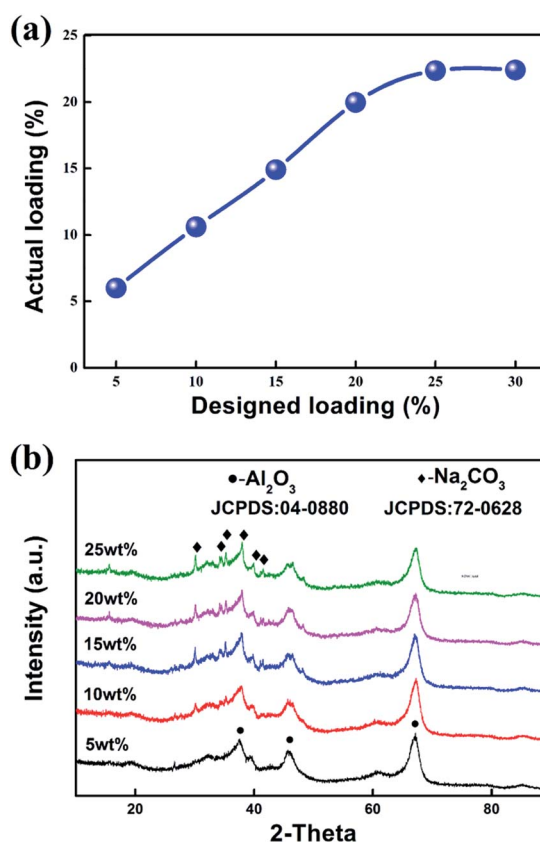


Fig. 3 (a) The curve of actual loading amount against the designed loading amount and (b) XRD patterns of the modified sorbents with different loading amounts: 0–25 wt%.

**Table 4** The BET results of the sorbents with different loading amounts

Loading amount (wt%)	Surface area (m <sup>2</sup> g <sup>-1</sup> )	Pore volume (cm <sup>3</sup> g <sup>-1</sup> )	Pore diameter (nm)
5	125	0.48	7.6
10	144	0.51	7.9
15	150	0.45	5.65
20	145	0.45	7.8
25	134	0.42	6.6

surface of the sample shows a small number of fibers growing along the edge of AAB pores, meanwhile blocking most of the fluffy structures. Further enhancing the loading amount to 15–20 wt%, the fibers on the surface of the samples reach their longest; that is, the fibers have an average length longer than 20  $\mu\text{m}$ , the average aspect ratio is more than 100, and they uniformly cover the surface of AABs, which greatly improves the active sites of sorbents. When the loading amount increased to 25 wt%, almost all the fibers disappeared, and the surface of AABs are covered completely by a thick layer of  $\text{Na}_2\text{CO}_3$ . The SEM results can explain the BET variation.

In order to analyze and understand the cause of formation and the phase composition of fibers, XRD, SEM and TEM of modified AABs with 15 wt% loading were subsequently detected. The EDS result in Fig. 4(e) shows that fibers consist of elements Na and Al, suggesting that  $\text{Na}_2\text{CO}_3$  may be adsorbed on the  $\text{Al}_2\text{O}_3$  substrate. Furthermore, detection of Al illustrates that the surface of the  $\text{Al}_2\text{O}_3$  substrate has not been completely enclosed, which benefits the effective utilization of the porous structure of the  $\text{Al}_2\text{O}_3$  substrate. Fig. 4(g) shows a typical TEM image of the fibers. The crystal plane distance measured by the lattice fringe is 0.237 nm or 0.238 nm in Fig. 4(h), which is similar to the (112) lattice spacing of  $\text{Na}_2\text{CO}_3$  (0.237 nm, PDF card no. 72-0628). Furthermore, it can be found that the  $\text{Na}_2\text{CO}_3$

fiber shows a stronger diffraction peak of (112) in Fig. 4(f), suggesting that the growth of fibers is oriented along the [112] direction.

The pore volume distribution of the six samples is shown in Fig. 5. It can be seen that the pore volume distribution of modified samples concentrates in the range of 5–10 nm and that the samples exhibit almost uniform mesoporous structure, which agrees well with the result of SEM observation.

**3.1.3 Effect of impregnation time.** The FESEM images of AABs modified at different durations (2 h, 10 h, 17 h and 24 h) in the impregnation solution and then dried at 473 K for 24 h are separately shown in Fig. 6. It shows that the surface morphology of the samples transformed obviously with prolonged impregnation time. When the impregnation time is less than 10 h, no  $\text{Na}_2\text{CO}_3$  fiber appears on the surface of the sample. The  $\text{Na}_2\text{CO}_3$  fibers achieve maximum and uniform coverage on the surface of AABs when the impregnation time reaches 17 h. When the

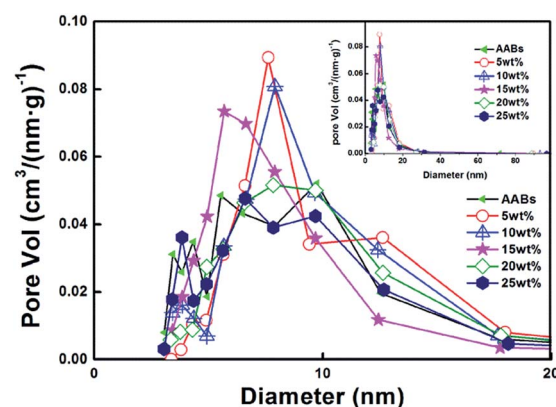


Fig. 5 Pore volume distribution of the modified sorbents with different loading amounts: 0–25 wt%, inset image is the full view of the pore volume distribution.

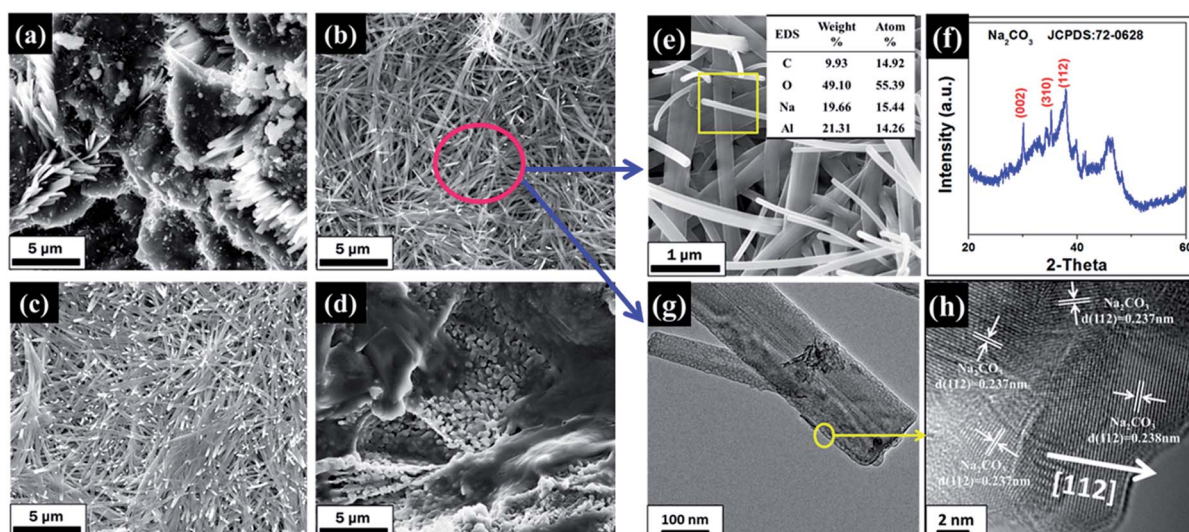


Fig. 4 Representative FESEM images of modified AABs with different loading amounts of  $\text{Na}_2\text{CO}_3$ : (a) 5 wt%, (b) 15 wt%, (c) 20 wt%, (d) 25 wt%, and (e) typical SEM-EDS analysis of the fibers, (f) XRD pattern of the modified AABs (15 wt%), and (g) TEM and (h) HRTEM images of the fiber.



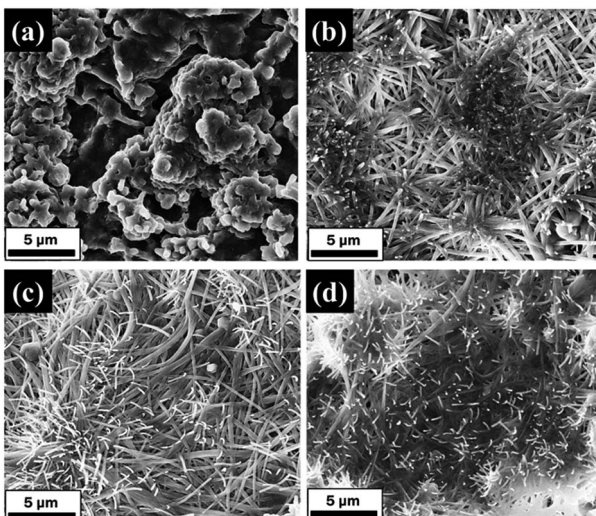


Fig. 6 FESEM images of modified AABs (20 wt%) with different impregnation time: (a) 2 h, (b) 10 h, (c) 17 h, (d) 24 h (impregnation conditions: drying for 24 h at 473 K).

impregnation time is more than 24 h, however, the  $\text{Na}_2\text{CO}_3$  fibers on the substrate surface bond together, suggesting that impregnation for too long a time inhibited the growth of  $\text{Na}_2\text{CO}_3$  fibers. Hence, the  $\text{Na}_2\text{CO}_3$  fibers on the surface of the modified AABs only appear with maximum and uniform coverage after 17 h impregnation.

**3.1.4 Effect of drying time.** After immersion in 20 wt%  $\text{Na}_2\text{CO}_3$  solution for 17 h, the sorbents were dried from 16 h to 28 h in an oven (423 K). Their microstructures are shown in Fig. 7. Similarly,  $\text{Na}_2\text{CO}_3$  fibers show obvious differences under different drying time. When the drying time is 16 h, the bud of the  $\text{Na}_2\text{CO}_3$  fibers just grew on the surface of the AABs. With prolonged drying time to 24 h, the  $\text{Na}_2\text{CO}_3$  fibers are also

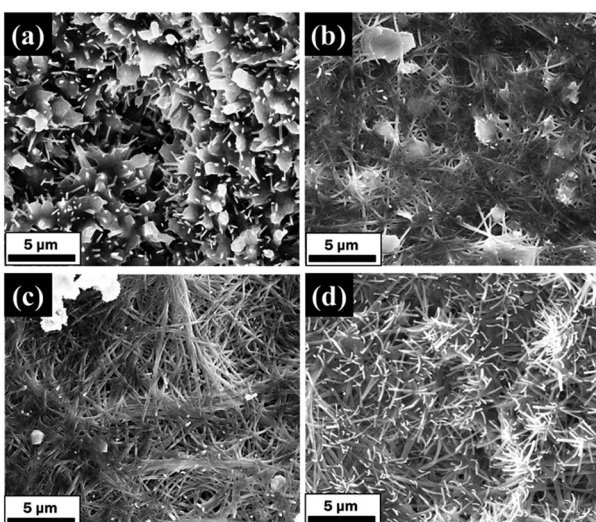


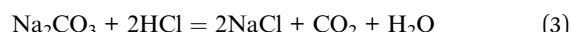
Fig. 7 FESEM images of modified AABs (20 wt%) at different drying time: (a) 16 h, (b) 20 h, (c) 24 h, (d) 28 h (impregnation conditions: impregnation time is 17 h, drying at 473 K).

observed on the surface of AABs. However, when the drying time is further extended, the  $\text{Na}_2\text{CO}_3$  fibers stopped further growth, suggesting that the production of fibers achieved equilibrium due to the complete exhaustion of moisture.

The wetness impregnation method was used to support  $\text{Na}_2\text{CO}_3$  on AABs to obtain the modified sorbents.  $\text{Na}_2\text{CO}_3$  fibers are controlled to grow on the AAB surface by adjusting the loading amount, the impregnation time and the drying time. The optimal conditions for fiber growth are a loading amount of 15–20 wt%, impregnation time of 17 h and drying at 473 K for 24 h.

### 3.2 HCl adsorption measurement

After the AABs were modified with the  $\text{Na}_2\text{CO}_3$  fibers, the HCl removal experiments were carried out. In this study, the principle of HCl removal is an acid–base reaction, as shown in eqn (3).



The capture of HCl involved firstly the physical selective adsorption on the surface of  $\text{Na}_2\text{CO}_3$  fibers, followed by the acid–base reaction, forming  $\text{NaCl}$  crystals on the sorbent surface along with  $\text{CO}_2$ , which escapes out.

The total conversion rate  $X_e$  of  $\text{Na}_2\text{CO}_3$  can be adopted to evaluate the reaction degree, which is depicted as eqn (4):

$$X_e = \frac{M_N(q_e - q_0)}{2 \times \frac{A}{1 + A} \times 1000} \quad (4)$$

where  $M_N$  is the molecular weight of  $\text{Na}_2\text{CO}_3$  (106 g mol<sup>-1</sup>),  $A$  (wt%) is the initial loading amount of  $\text{Na}_2\text{CO}_3$ ,  $q_0$  (mmol g<sup>-1</sup>) is the HCl adsorption capacity of the AABs, and  $q_e$  (mmol g<sup>-1</sup>) is the HCl adsorption capacity of the modified AABs.

**3.2.1 Reaction product analysis.** The surface morphology image of the exhausted sorbent with 20 wt% loading is obviously different from the original sorbents, as shown in Fig. 8(a). The elemental distribution of the energy spectrum, shown in Fig. 8(b), suggests that the phases on the surface of the sorbent are almost entirely  $\text{NaCl}$  and  $\text{Al}_2\text{O}_3$  (carbon had been sprayed for electrical conduction). The XRD patterns of exhausted sorbents are shown in Fig. 8(c); they contain the characteristic peak of  $\text{NaCl}$  besides the substrate, indicating again that the solid-phase product of the reaction is only  $\text{NaCl}$ .

**3.2.2 Adsorption efficiency analysis.** The pH evolution curves and the adsorption efficiency  $\eta$  curves of the sorbents with different loading amounts are shown in Fig. 9. It can be seen that the pH value is almost kept constant during the whole adsorption process for the AAB sorbents before breakthrough (Fig. 9(a)), indicating that the physical adsorption of HCl is efficient, with the breakthrough time of 37 min. However, the breakthrough time is significantly delayed with the increase of the  $\text{Na}_2\text{CO}_3$  loading amounts (Fig. 9(b)), suggesting that the adsorption performance has been improved by chemical adsorption, and the longest breakthrough time of 120 min is obtained with the loading amount of 20 wt% and 25 wt%. As shown in Fig. 9(c) of the enlarged curves, there is a clear

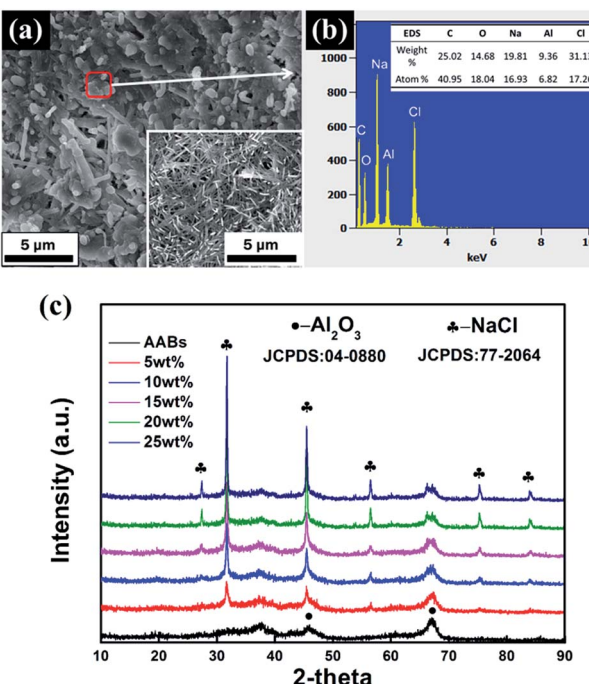


Fig. 8 (a) FESEM image and (b) typical EDS spectrum of the exhausted sorbent with 20 wt% loading; (c) XRD patterns of the exhausted sorbents with different loading amounts: 0–25 wt%. The inset image in (a) presents the original microstructure of the fibers.

reduction of pH value in the modified adsorbents, at which the physical adsorption is suppressed; meanwhile, the chemical reaction increases slowly, and it is named as transition time  $t_c$ . The breakthrough times  $t_b$  and transition times  $t_c$  are shown in Fig. 9(d).

The physical adsorption processes of these modified sorbents are far less than the AABs, suggesting that  $\text{Na}_2\text{CO}_3$  has blocked the original pores of AABs. When the neutralization reaction between HCl and  $\text{Na}_2\text{CO}_3$  is faster than the physical adsorption, the overall adsorption efficiency is only attributed to the chemical adsorption, where the sorbents completely capture the HCl. After the sorbent was consumed to a certain extent, HCl adsorption stopped, and the adsorption efficiency dropped dramatically (Fig. 9(b)); the sorbents became ineffective.

**3.2.3 Adsorption capacity analysis.** The HCl adsorptive capacity  $q_e$  and final conversion ratio of  $\text{Na}_2\text{CO}_3 X_e$  were calculated by eqn (1) and (4). The curves of  $q_e$  and  $X_e$  with different loading amounts of  $\text{Na}_2\text{CO}_3$  are shown in Fig. 10. It can be observed that the highest value of  $q_e$  reaches  $3.56 \text{ mmol g}^{-1}$ , which is five times the adsorption capacity of AABs. Meanwhile, it keeps a conversion ratio higher than 0.98 before the sorbents have been exhausted. When the loading amount increased to 25 wt%, the conversion ratio of  $\text{Na}_2\text{CO}_3$  decreased from 0.98 to 0.90. The conversion of the  $\text{Na}_2\text{CO}_3$  obtained in this study is higher than that of the previously reported ones in literature, summarized in Table 5.

**3.2.4 Kinetics of HCl adsorption.** In order to elucidate the reaction mechanism of HCl adsorption by AAB modified with

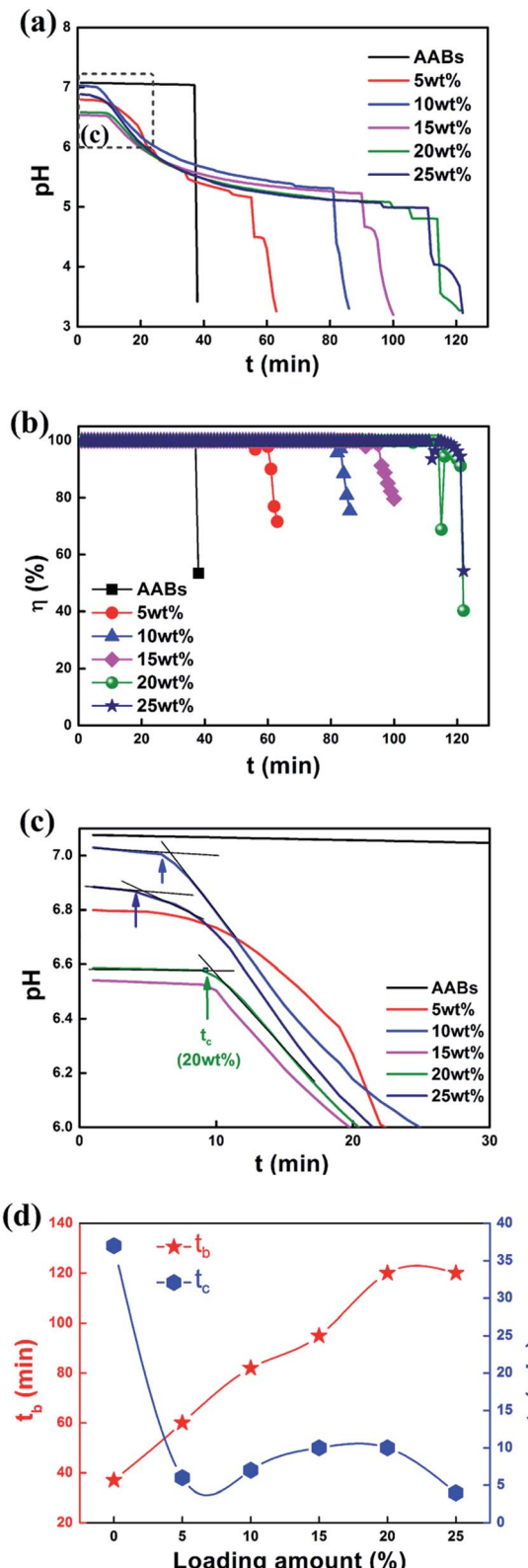


Fig. 9 (a) The pH evolution curves and (b) the adsorption efficiency  $\eta$  curves of the sorbents with different loading amounts: 0–25 wt%. (c) The enlarged curves of (a) in the early 30 min period; (d) the curves of breakthrough time  $t_b$  and transition time  $t_c$ .



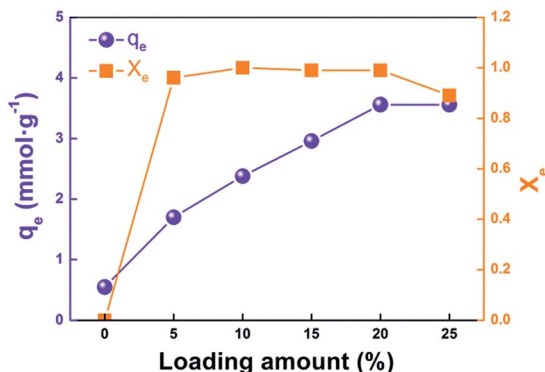


Fig. 10 The curves of adsorption capacity  $q_e$  and conversion ratio of  $\text{Na}_2\text{CO}_3 X_e$  vs. loading amounts.

$\text{Na}_2\text{CO}_3$  fibers, some models have been fitted to explain the kinetics of HCl adsorption at 423 K. The process of HCl adsorption can be divided into the following four steps:

- (1) The HCl gas adsorbs on the surface of the  $\text{Na}_2\text{CO}_3$  fibers.
- (2) HCl and  $\text{Na}_2\text{CO}_3$  molecules react on the surface of  $\text{Na}_2\text{CO}_3$  fibers, generating  $\text{H}_2\text{O}$ ,  $\text{NaCl}$  and  $\text{CO}_2$ .
- (3) The  $\text{CO}_2$  molecules escape outwardly into the gas stream through the product layer;  $\text{H}_2\text{O}$  molecules, combined with fresh HCl molecules, diffuse to the inside surface of unreacted fibers.
- (4) When the reaction rate of HCl and  $\text{Na}_2\text{CO}_3$  quickly reduces, the sorbents become exhausted.

In this study, the principle of HCl adsorption is shown in eqn (3). The conversion ratio with per-minute  $X_t$  can be calculated to investigate the kinetics of HCl adsorption, as shown in eqn (5):

$$X_t = X_e \times \frac{\int_{t_c}^t \eta dt}{\int_{t_b}^{t_c} \eta dt} \quad (t > t_c) \quad (5)$$

where  $X_e$  represents the maximum conversion rate, shown in Fig. 10,  $\eta$  (%) represents the adsorption efficiency of the sorbent at the time  $t$ ,  $t_b$  (min) is the breakthrough time of the sorbents, and  $t_c$  (min) is the transition time of the sorbents.

Considering the pore size distribution of the sorbent, the vast majority of the mesopores do not govern the entry or exit of the gas; that is, the external diffusion of the gas never becomes

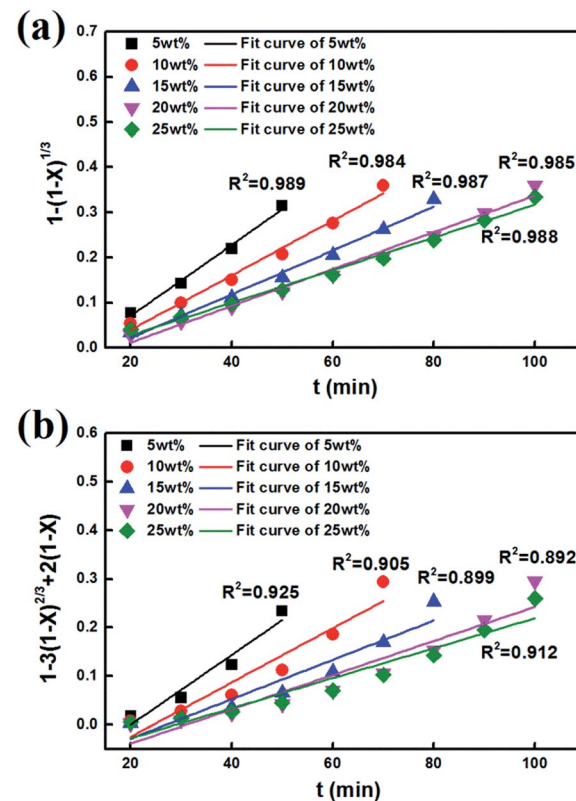


Fig. 11 Correlation of  $X$  with time  $t$ : (a) interfacial chemical reaction control, (b) product layer diffusion control.

the rate-limiting link of the adsorption reaction. According to the previous reports,<sup>42–46</sup> the reaction kinetics of sorbents and HCl in the reaction of HCl adsorption at high temperature is mainly controlled by diffusion in the product layer or interfacial chemical reaction.

If reaction is controlled by the interfacial chemical reaction at the grain surface, it will follow eqn (6):<sup>9,13,44</sup>

$$g(X) = 1 - (1 - X)^{\frac{1}{3}} = K_1 t \quad (6)$$

where  $t$  is the reaction time and  $K_1$  represents the reaction rate constant.

Table 5 Comparison of adsorption temperature and breakthrough performance with reported literatures<sup>a</sup>

Adsorbent	Percentage of active components	Gas flow rate (mL min⁻¹)	Adsorption T (K)	Breakthrough HCl capacity/mmol g⁻¹	Conversion rate	Ref.
$\text{Na}_2\text{CO}_3 \cdot 10\text{H}_2\text{O}$	—	250	673–773	—	0.49	5
$\text{Ca}(\text{OH})_2$	—	150	443	—	~0.15	15
Limestone/	30 wt%	1400	1123	—	~0.6	16
$\text{Al}_2\text{O}_3$	—	3000 (h⁻¹) <sup>α</sup>	823	4.1	~0.4	14
CN1 <sup>#</sup>	—	100	308	0.05	—	36
$\text{NaOH/AC}^{\$}$	8 wt%	100	308	0.33	—	36
$\text{Na}_2\text{CO}_3/\text{AC}^{\$}$	5 wt%	500	673	6.28	0.75	29
$\text{K}_2\text{CO}_3/\text{Al}_2\text{O}_3$	40 wt%	40	423	3.56	0.98	This study
$\text{Na}_2\text{CO}_3/\text{Al}_2\text{O}_3$	20 wt%	—	—	—	—	—

<sup>a</sup> CN1<sup>#</sup> is  $\text{Na}_{0.98}\text{Mg}_{0.25}\text{Ca}_{2.3}\text{O}_{3.04}$ , mixed with binders and texturing agents.  $\text{AC}^{\$}$  is activated carbon. (h⁻¹)<sup>α</sup> is the unit of space velocity.



If the reaction is controlled by reactant diffusion through the product layer, it will follow eqn (7):

$$p(X) = 1 - 3(1 - X)^{\frac{2}{3}} + 2(1 - X) = K_2 t \quad (7)$$

where  $K_2$  represents the reaction rate constant.

After fitting the experimental data to eqn (6) and (7), the calculated results are separately shown in Fig. 11(a) and (b). Compared with correlation coefficient, the figure shows that the model of the interfacial chemical reaction control could better explain the experimental results; especially, the linear fitting coefficient  $R^2$  of the modified AABs is larger than 0.980, proving that the adsorption reaction is completely controlled by the interfacial chemical reaction. On one hand, the  $\text{Na}_2\text{CO}_3$  fibers did not block the fluffy structures on the surface of original AABs as shown in Fig. 2(b) and maintained the large specific surface area of the AABs; on the other hand, the uniform pore distribution of  $\text{Na}_2\text{CO}_3$  fibers provided many convenient channels for the gas inward and outward, both resulting in the easier diffusion of gas phase in the product layer. In this case, internal diffusion of gas phase will no longer be the rate-limiting step in the process of chemical adsorption.

## 4. Conclusions

In this paper, alkali-modified AABs have been prepared to evaluate their performance for HCl adsorption at low temperature (423 K). The results have demonstrated better modification ability of  $\text{Na}_2\text{CO}_3$  compared to  $\text{Ca}(\text{OH})_2$  or  $\text{NaOH}$ . A typical fibrous structure was obtained on the surface of the sorbent by loading  $\text{Na}_2\text{CO}_3$ . The loading amounts, impregnation time and drying time had great impact on the morphology of  $\text{Na}_2\text{CO}_3$  fibers. When the loading amount was 15–20 wt%, the impregnation time was 17 h, and the drying time was 24 h,  $\text{Na}_2\text{CO}_3$  fibers with good orientation and high aspect ratio could be obtained.

In addition, the HCl adsorption performance was investigated in a fixed bed reactor at 423 K. Extremely high adsorption efficiency and the highest adsorption capacity of 3.56 mmol HCl g<sup>-1</sup> were achieved when the loading amount was 20 wt%; the adsorption capacity of the modified sorbents is five times that of AABs. The physical adsorption is faster than chemical adsorption in the initial process of HCl adsorption, and then the dominant reaction strongly depends on the chemical adsorption. The kinetics investigation indicates that the reaction is controlled by the interfacial chemical reaction; the diffusion of gas phase in the product layer has been greatly improved by the fiber structure. We believe that  $\text{Na}_2\text{CO}_3$  fiber-impregnated AABs are promising for the commercial application of HCl removal from BFG.

## Conflicts of interest

There are no conflicts to declare.

## Acknowledgements

This work was financially supported by the National Natural Science Foundation of China (51672025, 51572020, 51372019),

and Major Projects of Science and Technology in Shanxi Province (MC2016-03).

## Notes and references

- K. Goto, H. Okabe, F. A. Chowdhury, S. Shimizu, Y. Fujioka and M. Onoda, *Int. J. Greenhouse Gas Control*, 2011, **5**, 1214–1219.
- B. S. Hu, Y. L. Gui, G. Y. Hu, K. Lv and C. Y. Song, *Environ. Eng.*, 2016, **34**, 78–80.
- B. Zhang, B. S. Hu, Y. L. Gui, X. G. Liu and G. Y. Hu, *Mod. Chem. Ind.*, 2016, **36**, 137–140.
- R. Bie, S. Li and L. Yang, *Chem. Eng. Sci.*, 2005, **60**, 609–616.
- W. Duo and N. F. Kirkby, *Chem. Eng. Sci.*, 1996, **51**, 2541–2546.
- A. D. Lawrence and J. Bu, *Chem. Eng. Sci.*, 2000, **55**, 6129–6137.
- W. Duo, N. F. Kirkby, J. P. K. Seville and R. Clift, *Chem. Eng. Sci.*, 1995, **50**, 2017–2027.
- H. Matsuda, S. Ozawa, K. Naruse, K. Ito, Y. Kojima and T. Yanase, *Chem. Eng. Sci.*, 2005, **60**, 545–552.
- B. L. Dou, C. Wang, H. S. Chen, Y. C. Song, B. Z. Xie, Y. J. Xu and C. Q. Tan, *Chem. Eng. Res. Des.*, 2012, **90**, 1901–1917.
- G. M. Lin and C. S. Chyng, *Energy Fuels*, 2016, **30**, 10696–10704.
- M. Nunokawa, M. Kobayashi and H. Shirai, *Powder Technol.*, 2008, **180**, 216–221.
- W. Duo, J. P. K. Seville, N. F. Kirkby and R. Clift, *Chem. Eng. Sci.*, 1994, **49**, 4429–4442.
- B. L. Dou, B. B. Chen, J. S. Gao and X. Z. Sha, *Energy Fuels*, 2005, **19**, 2229–2234.
- B. Dou, W. Pan, J. Ren, B. Chen, J. Hwang and T.-U. Yu, *Energy Fuels*, 2007, **21**, 1019–1023.
- R. Yan, T. Chin, D. T. Liang, K. Laursen, W. Y. Ong, K. Yao and J. H. Tay, *Environ. Sci. Technol.*, 2003, **37**, 2556–2562.
- J. Partanen, P. Backman, R. Backman and M. Hupa, *Fuel*, 2005, **84**, 1664–1673.
- C. Yang, L. L. Gao, Y. X. Wang, X. K. Tian and S. Komarneni, *Microporous Mesoporous Mater.*, 2014, **197**, 156–163.
- Z. R. Zhang, R. W. Hicks, T. R. Pauly and T. J. Pinnavaia, *J. Am. Chem. Soc.*, 2001, **124**, 1592–1593.
- T. J. Bandosz, *Carbon*, 1999, **37**, 483–491.
- M. Balsamo, S. Cimino, G. de Falco, A. Erto and L. Lisi, *Chem. Eng. J.*, 2016, **304**, 399–407.
- M. C. Castrillon, K. O. Moura, C. A. Alves, M. Bastos-Neto, D. C. S. Azevedo, J. Hofmann, J. Möllmer, W.-D. Einicke and R. Gläser, *Energy Fuels*, 2016, **30**, 9596–9604.
- A. Taguchi and F. Schüth, *Microporous Mesoporous Mater.*, 2005, **77**, 1–45.
- W. Feng, S. Kwon, E. Borguet and R. Vidic, *Environ. Sci. Technol.*, 2005, **39**, 9744–9748.
- R. Yan, D. T. Liang, L. Tsen and J. H. Tay, *Environ. Sci. Technol.*, 2002, **36**, 4460–4466.
- L. Li, T. H. Sun, C. H. Shu and H. B. Zhang, *J. Hazard. Mater.*, 2016, **311**, 142–150.
- J. Y. Kim, Y. C. Park, S. H. Jo, H. J. Ryu, J. I. Baek and J. H. Moon, *Energy Fuels*, 2016, **30**, 2268–2275.



27 G. J. McIntosh, G. E. Agbenyegah, M. M. Hyland and J. B. Metson, *Langmuir*, 2015, **31**, 5387–5397.

28 D. Dayananda, V. R. Sarva, S. V. Prasad, J. Arunachalam, P. Parameswaran and N. N. Ghosh, *Appl. Surf. Sci.*, 2015, **329**, 1–10.

29 S. J. Park and S. Y. Jin, *Carbon*, 2004, **42**, 2113–2115.

30 B. Tu, N. Shi, W. Sun, L. Cao and J. Yang, *Environ. Sci. Pollut. Res.*, 2017, **24**, 676–684.

31 W. Dong, X. Chen, F. Yu and Y. Wu, *Energy Fuels*, 2015, **29**, 968–973.

32 A. G. Skerman, S. Heubeck, D. J. Batstone and S. Tait, *Process Saf. Environ. Prot.*, 2017, **105**, 117–126.

33 A. Daneshyar, M. Ghaedi, M. M. Sabzehei and A. Daneshyar, *J. Colloid Interface Sci.*, 2017, **490**, 553–561.

34 M.-T. Lee, Z.-Q. Wang and J.-R. Chang, *Ind. Eng. Chem. Res.*, 2003, **42**, 6166–6170.

35 L. Micoli, G. Bagnasco and M. Turco, *Int. J. Hydrogen Energy*, 2014, **39**, 1783–1787.

36 L. Micoli, G. Bagnasco and M. Turco, *Int. J. Hydrogen Energy*, 2013, **38**, 447–452.

37 C. Zhao, X. Chen and C. Zhao, *Energy Fuels*, 2012, **26**, 1401–1405.

38 C. Zhao, Y. Guo, C. Li and S. Lu, *Appl. Energy*, 2014, **124**, 241–247.

39 C. Zhao, X. Chen and C. Zhao, *Chemosphere*, 2009, **75**, 1401–1404.

40 B. Y. Zhao, D. E. Jiang and Y. C. Xie, *Fuel*, 2002, **81**, 1565–1568.

41 W. Dong, X. Chen, Y. Wu, C. Zhao and C. Liang, *Energy Fuels*, 2012, **26**, 6040–6046.

42 N. Verdone and P. D. Filippis, *Chem. Eng. Sci.*, 2006, **61**, 7487–7496.

43 A. M. Fonseca, J. J. Órfão and R. L. Salcedo, *Ind. Eng. Chem. Res.*, 1998, **37**, 4570–4576.

44 B. L. Dou, J. S. Gao and X. Z. Sha, *Fuel Process. Technol.*, 2001, **72**, 23–33.

45 M. J. D. Low, *Chem. Rev.*, 1980, **60**, 267–312.

46 C. E. Weinell, P. I. Jensen and K. D. Johansen, *Ind. Eng. Chem. Res.*, 1992, **31**, 164–171.

